

## RESEARCH ARTICLE

### Flexible strategies for flight control: an active role for the abdomen

Jonathan P. Dyhr<sup>1,\*</sup>, Kristi A. Morgansen<sup>2</sup>, Thomas L. Daniel<sup>1</sup> and Noah J. Cowan<sup>3</sup>

<sup>1</sup>University of Washington, Department of Biology, 24 Kincaid Hall, Seattle, WA 98195-1800, USA, <sup>2</sup>Department of Aeronautics and Astronautics, University of Washington, 211 Guggenheim Hall, Box 352400, Seattle, WA 98195-2400, USA and <sup>3</sup>Department of Mechanical Engineering, Johns Hopkins University, 126 Hackerman Hall, 3400 N. Charles Street, Baltimore, MD 21218, USA

\*Author for correspondence (jdyhr@u.washington.edu)

#### SUMMARY

Moving animals orchestrate myriad motor systems in response to multimodal sensory inputs. Coordinating movement is particularly challenging in flight control, where animals deal with potential instability and multiple degrees of freedom of movement. Prior studies have focused on wings as the primary flight control structures, for which changes in angle of attack or shape are used to modulate lift and drag forces. However, other actuators that may impact flight performance are reflexively activated during flight. We investigated the visual–abdominal reflex displayed by the hawkmoth *Manduca sexta* to determine its role in flight control. We measured the open-loop stimulus–response characteristics (measured as a transfer function) between the visual stimulus and abdominal response in tethered moths. The transfer function reveals a 41 ms delay and a high-pass filter behavior with a pass band starting at ~0.5 Hz. We also developed a simplified mathematical model of hovering flight wherein articulation of the thoracic–abdominal joint redirects an average lift force provided by the wings. We show that control of the joint, subject to a high-pass filter, is sufficient to maintain stable hovering, but with a slim stability margin. Our experiments and models suggest a novel mechanism by which articulation of the body or ‘airframe’ of an animal can be used to redirect lift forces for effective flight control. Furthermore, the small stability margin may increase flight agility by easing the transition from stable flight to a more maneuverable, unstable regime.

Supplementary material available online at <http://jeb.biologists.org/cgi/content/full/216/9/1523/DC1>

Key words: abdominal deflection, biomechanics, flight control, *Manduca sexta*, system identification, vision.

Received 23 July 2012; Accepted 22 December 2012

#### INTRODUCTION

Flying animals are capable of precise, agile maneuvers that range from hovering while feeding from a moving flower, to mating in midair, to the complex interactions between aerial predators and prey. Flight control requires sensory inputs from a diversity of modalities and the coordination of multiple muscles across the body. The difficulty of experimentally disentangling the interactions between sensors, muscles and the physical dynamics of the body has led many studies to focus on understanding movement through the action of a single, primary motor output. This single output approach is particularly true in the case of flight, where the production of lift and thrust forces by the wings makes them obvious targets for study (Taylor, 2001).

Because of the crucial importance of the wings, less attention has been paid to the role of body shape, or the ‘airframe’ of the animal, for flight control. Changes in the shape of the body of an animal can alter the relative positions of the center of pressure on the body or its center of mass relative to the center of lift and thrust produced by wings. Thus the body itself could be a key contributor to the system of actuators involved in flight control, exercising ‘airframe-based’ control. Indeed, the control potential of body shape has been established for the passive, aerial descent paths of terrestrial lizards (Libby et al., 2012), but not for flying animals.

The clearest evidence for airframe-based control comes from insects, where strong abdominal steering reflexes occur in response to visual or mechanical sensory stimuli. Desert locusts (*Schistocerca*

*gregaria*), for example, respond with large abdominal and leg motions when presented with angled wind stimuli during tethered flight (Camhi, 1970a; Camhi, 1970b). Similar responses have been observed in fruit flies (*Drosophila melanogaster*) in response to visual rotations (Götz et al., 1979; Zanker, 1988a; Zanker, 1988b). These abdominal responses depend on the axis of stimulation, with the yaw rotations eliciting strong horizontal abdominal movements and the pitch rotations prompting vertical movements. Moths (*Manduca sexta*) display strong abdominal responses to both visual and mechanical rotations about the pitch axis (Hinterwirth and Daniel, 2010). In addition, honeybees (*Apis mellifera*) modulate the vertical abdominal angle based on the speed of a translating visual pattern (Luu et al., 2011).

Proposed mechanisms for control by abdominal flexion include: (1) its role as an aerodynamic rudder, moving the center of drag relative to the center of lift, leading to either increased moments due to decreased streamlining (Camhi, 1970a; Zanker, 1988a) or decreased moments via greater streamlining (Luu et al., 2011); and (2) deformations of the body (airframe) will shift the center of mass relative to the center of lift, affecting a pitch or yaw moment that can be used for flight control (Dyhr et al., 2012; Hedrick and Daniel, 2006; Zanker, 1988a).

Here we develop a control theoretic approach (Fig. 1), which integrates sensory mediated changes in abdominal position with modeled body dynamics, to understand the effectiveness of airframe shape changes for governing the flight path of an insect. Using a

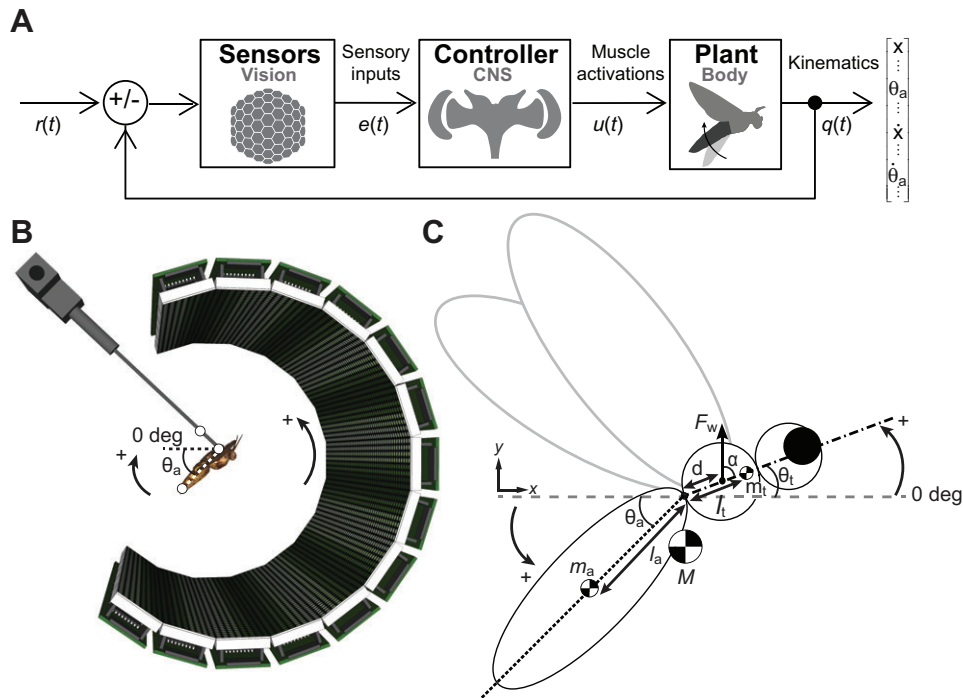


Fig. 1. Experimental design and feedback diagram. (A) The flow of information underlying the visual–abdominal reflex was envisaged as a feedback control system, where time-dependent signals (arrows) are filtered (boxes) to produce a kinematic output. Visual sensors detect the motion of the animal,  $q(t)$ , relative to the environment,  $r(t)$ , to produce a motion-dependent ‘error’ signal,  $e(t)$ . The error signal is processed by central nervous system (CNS) to generate an appropriate behavioral response by sending signals,  $u(t)$ , to the muscles. The actions of the muscles are filtered by the body dynamics, or plant, to yield a kinematic output in the form of state variables (e.g.  $x$ ,  $\theta_a$ ). (B) The sensor and controller processing blocks of the visual–abdominal reflex were characterized by presenting visual pitch rotations to tethered moths in a cylindrical LED arena. The abdominal angle ( $\theta_a$ ) was measured relative to the horizontal axis using three tracking points (white circles): two fixed points on the tether and one moving point painted on the abdomen. (C) The dynamics of the plant were derived using a simple physical model of the moth composed of two masses, corresponding to the abdomen and the thorax, connected by a hinge joint. The abdomen and thorax both had fixed masses,  $m_a$  and  $m_t$ , at distances  $l_a$  and  $l_t$  from the hinge joint. The head was included as part of the thorax. The centers of mass of each body segment, as well as of the two-body system ( $M$ ), are denoted by the checkered circles. The angles of the major axes of the abdomen and thorax ( $\theta_a$  and  $\theta_t$ ) were defined relative to the horizontal (gray dashed line). The action of the wings was simulated with an average lift force ( $F_w$ , vertical arrow), located at a distance  $d$  from the hinge joint and oriented at an angle  $\alpha$  relative to  $\theta_t$ . Abdominal flexion was implemented as a torque,  $\tau$ , on the hinge joint modulating  $\theta_a$  and  $\theta_t$ .

systems identification approach following methods developed by Roth et al. (Roth et al., 2011), we seek to quantify the system stability (or conversely agility).

We suggest that, in addition to shifting the center of mass, airframe morphing provides a mechanism for redirecting lift forces to control flight *via* conservation of angular momentum. Inspiration for the mechanism came from tethered flight experiments of the visual–abdominal reflex in the hawkmoth *Manduca sexta*. By presenting the moths oscillating vertical patterns with broadband temporal frequency content we found that abdominal motions were, to a good approximation, linear and time invariant with respect to the visual input. We then estimated the open-loop transfer function from pitch rotations of the visual field to dorsal–ventral abdominal flexion. The effectiveness of these abdominal movements for maintaining pitch stability in free flight was then tested using a mathematical model of a hovering moth. Our results demonstrate that the experimentally measured abdominal movements are sufficient for maintaining stable hovering flight, suggesting that moths actively alter body shape to control flight. Furthermore, they operate near the edge of stability where minor perturbations will move them into an unstable and more maneuverable configuration with much higher available rates of change for switching between states.

## MATERIALS AND METHODS

### Animals

*Manduca sexta* (Linnaeus) were reared in the Department of Biology at the University of Washington, Seattle. A total of 10 moths of both sexes were used for experiments 3–5 days after eclosion. Prior to experiments, moths were secured to a metal rod *via* a magnet glued to the dorsal thorax (Hinterwirth and Daniel, 2010). For a subset of experiments (two moths), the head was restrained by bridging the UV-cured glue from the tether base to the top of the head. The tether was adjusted to maintain a 45 deg body angle during flapping flight. Abdominal position was measured using high-speed digital video *via* a tracking point painted onto the tip of the abdomen. Animals were tested after they had warmed up by flying on the tether at least 1 min.

### Flight arena

A wrap-around LED display system (Reiser and Dickinson, 2008) spanning the moth’s visual field  $\pm 110$  deg vertically and  $\pm 50$  deg horizontally was used to present visual stimuli (Fig. 1B). Moths were dark adapted for at least 30 min prior to experiments. A neutral density filter was placed over the LEDs to reduce the average light level reaching the moth to a maximum of  $12 \text{ cd m}^{-2}$  (Gossen Mavolux 5032C luminance meter, Nürnberg, Germany) to keep

moths in a dark-adapted state, matching previous electrophysiological and behavioral studies in *M. sexta* (Hinterwirth and Daniel, 2010; Theobald et al., 2010). The visual image was controlled by signals generated in MATLAB (MathWorks, Natick, MA, USA) and output through a USB data acquisition board (USB 6251, National Instruments, Austin, TX, USA).

#### Data acquisition

Moth behavioral responses were captured from a lateral view at 186 frames s<sup>-1</sup> with a high-speed camera (Basler Pilot GigE, Basler Vision Technologies, Ahrensburg, Germany). The LED arena voltage output was used to reconstruct the visual stimulus and was recorded at 10 kHz using an USB data acquisition board (USB 6251, National Instruments). Simultaneously recorded frame synchronization pulses from the camera were used to temporally align the video data with the stimulus position information. A second USB data acquisition board (USB 6008, National Instruments) provided an automatic camera end-trigger, as well as a pulse signal for an infrared LED to confirm frame alignment. Abdominal position data were digitized from the image with the DLTdataviewer MATLAB software package (Hedrick, 2008). Abdominal deflection was quantified from the angle between the tether and abdomen tip for each frame (Fig. 1B).

#### Visual stimuli

The visual pattern consisted of a horizontally oriented square wave grating with a spatial frequency of 0.03 cycles deg<sup>-1</sup>. This frequency falls within the electrophysiologically measured spatial frequency optima of the motion sensitive lobula plate tangential neurons at low light levels in *M. sexta* (Theobald et al., 2010). Visual stimuli were oscillated vertically to mimic visual rotations in the pitch axis. The temporal dynamics of the motion were chosen to cover a broad range of temporal frequencies and consisted of two classes of stimuli: sum of sines and chirps.

The sum of sines stimuli were composed of 10 time-varying sinusoids that spanned more than two decades in temporal frequency, from 0.01 to 20 Hz (Fig. 2A). Using a method similar to that of Roth et al. (Roth et al., 2011), stimuli were generated by selecting 20 approximately logarithmically spaced frequencies that were all prime multiples of 0.05 Hz, to avoid interference from harmonics. The lowest frequency was 0.1 Hz and the highest was ~20 Hz. These frequencies were used to create component sinusoids, each with a random initial phase. The 20 components were split into two spectrally interlaced groups of 10, yielding two groups that approximately spanned the full frequency range. The maximum velocities of the individual components were normalized by scaling the position amplitude inversely with frequency. The sinusoids within a group were summed to yield a full sum of sines stimulus. The full stimuli were then normalized to a fixed maximum velocity in order to match velocity amplitude across trials. Amplitude was varied by multiplying the normalized sum of sines stimuli by a fixed scale factor. Each stimulus was generated separately, such that the randomized phases of the component sinusoids were different for a given amplitude and frequency range. However, the same stimuli were used across animals.

The sum of sines stimuli concentrated power at single frequencies, thereby increasing the signal-to-noise ratio, but resulting in relatively coarse frequency resolution. Furthermore, an additional 40 s sum of sines trial was necessary to acquire the full frequency spectrum at single amplitudes. Chirp stimuli (Fig. 2B), in which the instantaneous temporal frequency was increased continuously over time, provided higher-resolution frequency spectrums in a single 40 s trial. Hence,

chirps provided an efficient means of measuring abdominal responses at different stimulus amplitudes, but at the cost of a lower signal-to-noise ratio. In addition, consistency in the abdominal response across stimulus types provided a measure of the linearity of the behavioral responses.

Chirp stimuli (Fig. 2B) consisted of sinusoidally oscillating patterns with temporal frequencies that increased logarithmically over time. The logarithmic sweep signal, ranging from 0.1 to 16 Hz, was generated using the MATLAB chirp function (Signal Processing Toolbox). The maximum frequency was lower than for the sum of sines because tethered flight was not consistently maintained when moths were presented isolated high-frequency oscillations. In addition, the low signal-to-noise ratio of the chirp was problematic at high frequencies (>17 Hz) because of the high-powered noise from the wing beats. The maximum velocity of the chirp was normalized across frequencies. Unlike the sum of sines, normalizing the velocity of the final chirp stimulus was not necessary because only one frequency was present at any one time. The final amplitudes of the chirp stimuli were scaled to allow for comparison with the sum of sines. The gain factor was chosen by matching the summed power of the chirp within logarithmically spaced frequency bands to the power of the sum of sines stimuli.

#### Experimental trials

Moths were presented with seven 40 s stimulus presentations in each experimental trial: two different amplitudes of the two interlaced sum of sines stimuli and three different amplitudes of the chirp stimulus. The order of presentation was generated pseudo-randomly for each trial. The grating was held stationary for 200 ms at the beginning and end of each stimulus. Not all moths behaved over the full course of a full experiment. Trials during which a moth ceased flying, or had a wing-beat frequency less than 17 Hz, were not used for analysis.

#### Data analysis

Data analysis was performed in MATLAB. The voltage signal from the arena, specifying angular position, was downsampled using the camera frame-sync pulses and temporally aligned with the abdominal response data. Characterization of the visual-abdominal response was performed in frequency space by first calculating the discrete Fourier transform (DFT; calculated using MATLAB's `fft` command) of both the visual stimulus and the abdominal response. Magnitude was calculated by taking the absolute value of the DFT, while phase was calculated using the MATLAB `angle` function.

For the sum of sines trials, gain and phase were calculated only at the frequency maxima present in the visual stimulus. For chirps, the limited time duration of the stimulus at any given frequency resulted in a noisier signal at each discrete frequency. To overcome this effect, the DFT was averaged within 26 logarithmically increasing bins, and the magnitude and phase were calculated for each bin.

For Bode plots, gain was calculated by taking the ratio of the absolute value of the DFT of the response and the stimulus at each frequency. The phase lag was calculated by taking the difference of the response phase relative to the stimulus phase. Gain was calculated for each trial (on a decibel scale) after which the mean and confidence intervals were calculated for all moths. Phase was similarly averaged, but because the phase data were periodic, the mean and confidence intervals were calculated using the open source Circular Statistics Toolbox (Berens, 2009).

An alternative method for determining the gain and phase is to first average the complex valued frequency domain data and then

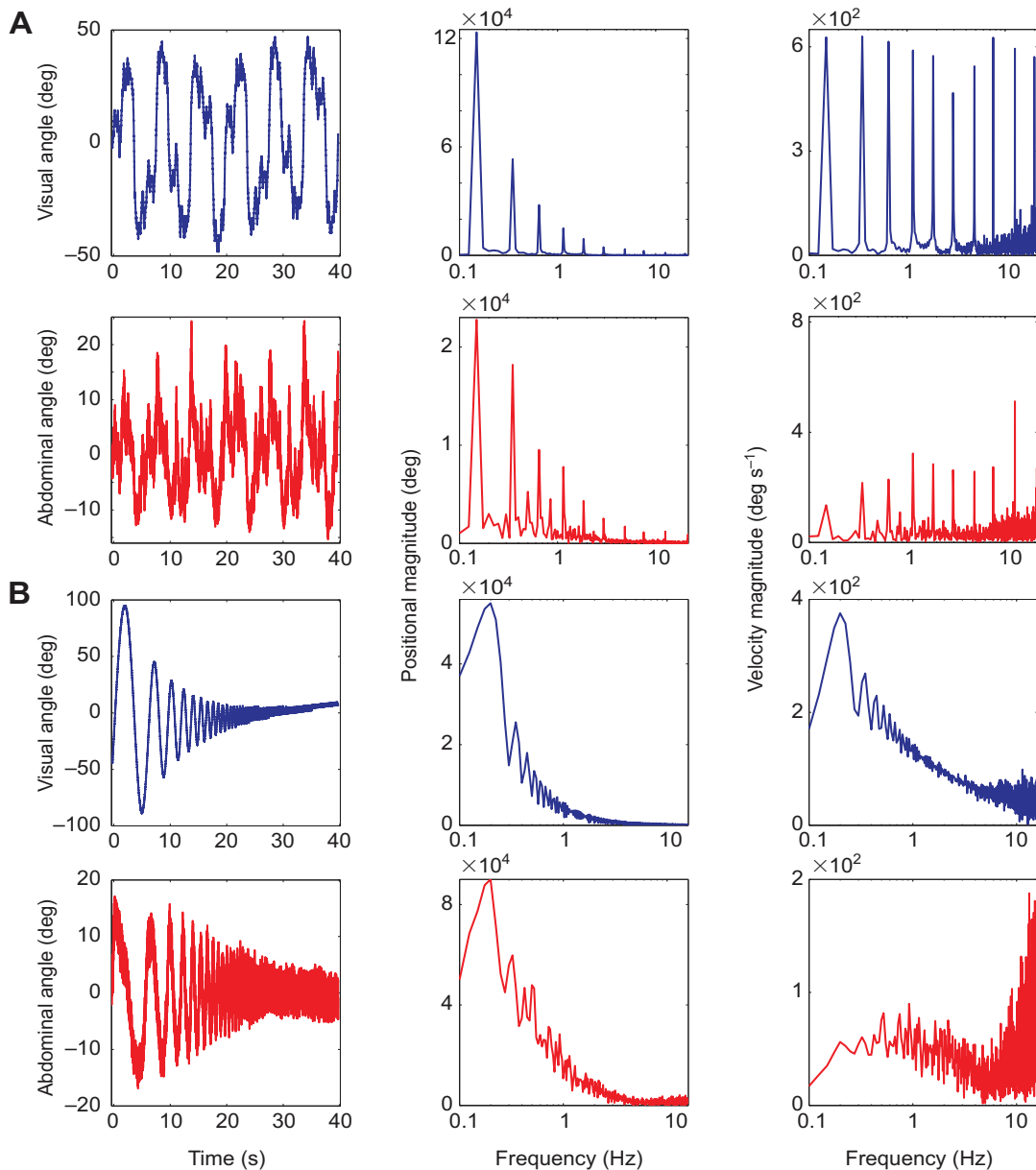


Fig. 2. Frequency selectivity of abdominal responses. (A) Example stimulus (top, blue) and abdominal response (bottom, red) from a single sum of sines experimental trial. The time-domain positional signal (left), Fourier transform of the position signal (middle) and the Fourier transform of the velocity (right) are shown for both the stimulus and response. Fourier transforms of the stimulus position and response illustrate the selectivity of the abdominal response. The 10 peaks in the stimulus correspond to the 10 different sinusoidal components of the sum of sines stimulus. The smaller peaks present only in the abdominal response trace are likely due to harmonics of the base frequency responses. The normalization of the sinusoidal components in velocity can be seen from the Fourier velocity plot (top right). Small differences in the peak heights are likely due to imperfect sampling. (B) Example signals for a chirp trial, same as above. Note that while the velocity of the chirp stimulus was normalized to a maximum value, the velocity magnitude of the stimulus in Fourier space has a negative slope (top right). This result is partially due to the logarithmic frequency ramping of the chirp stimulus that results in a higher density of samples at higher frequencies.

calculate the magnitude and phase angle to determine the gain and phase, respectively. The confidence intervals can then be calculated by fitting a Gaussian probability density function to the data in the complex plane (Roth et al., 2011). Both methods yield consistent results, with the results from the second averaging method reported in supplementary material Fig. S1.

#### Linearity estimates and time invariance

Specialized analytical tools for linear time-invariant systems allow for the precise determination of the long-term behavior of the

system. We tested whether the visual–abdominal response satisfied the linear conditions of superposition and scaling. In addition, we performed another linearity test, the signal–response coherence. These linearity measures implicitly tested the time invariance of the system.

Linear superposition requires that the outputs of a system to specific frequency inputs be equivalent regardless of whether the frequencies are presented individually or together. Chirp stimuli approximate single sinusoids presented serially over time, while the sum of sines stimuli presented multiple frequency components

simultaneously. Hence, consistency in the chirp and sum of sines responses would strongly suggest that the visual–abdominal response satisfies the linear superposition condition.

Linear scaling requires the output of the system to scale proportionally with the input. For the present study, this scaling required that the gain of the abdominal response be independent of visual signal amplitude. However, because all biological systems can be pushed outside of a linear range due to response saturation, we attempted to identify a limited range of amplitude within which responses were linear. Stimuli with three different maximum velocities were used: 225, 450 and 675 deg s<sup>-1</sup>. Following Roth et al. (Roth et al., 2011), velocity amplitude, as opposed to positional amplitude, was limited to prevent response saturation at high frequencies, thereby avoiding potential confounds between the frequency and velocity dependence of the responses. The velocity maxima were chosen empirically because moths did not maintain consistent tethered flight when the maximum velocity amplitude dropped below 225 deg s<sup>-1</sup>.

A final test of linearity was provided by the signal–response coherence (Bendat and Piersol, 1980; Roth et al., 2011). The coherence,  $C_{xy}$ , of two signals, an input  $x(t)$  and output  $y(t)$ , is defined as:

$$C_{xy} = \frac{|G_{xy}|^2}{G_{xx}G_{yy}}, \quad (1)$$

where  $G_{xx}$  and  $G_{yy}$  are the autospectral densities of  $x(t)$  and  $y(t)$ , respectively, and  $G_{xy}$  is the cross-spectral density of the two signals. The coherence provides a linear estimate of the relative power transfer from the input to the output, with  $0 \leq C_{xy} \leq 1$ . A coherence of 1 indicates that the spectral power transfer between the two systems is equal to the total power in the individual signals and can be completely explained by a linear transfer function between input and output. Low coherence can be due to multiple factors, including noise, nonlinearity or other inputs. However, it is important to note that high coherence is not a sufficient condition for linearity. A periodically excited nonlinear system will yield a coherence of 1 at the excited frequencies in the absence of noise (McCormack et al., 1994).

#### Model fit

The transfer function from image position to abdominal angle was determined by fitting the complex-valued frequency domain data with a first-order high-pass filter with a fixed time delay. We evaluated the goodness-of-fit of the model by calculating the  $\chi^2$  in the frequency domain as follows:

$$\chi^2 = \sum_{k=1}^n \frac{|\bar{O}(\omega_k) - G(\omega_k, \Theta)|^2}{\sigma_k^2}, \quad (2)$$

where  $\bar{O}(\omega_k)$  is the experimentally observed mean value at frequency  $\omega_k$  and  $G(\omega_k, \Theta)$  is the value predicted by the modeled transfer function with parameters  $\Theta$  (Taylor, 1997). For the variance term  $\sigma_k^2$  we used the squared standard error of the mean, calculated as the trace of the covariance matrix of the observed data points at each frequency (Pintelon and Schoukens, 2012) divided by the number of samples at each frequency. This type of least squares fitting will yield biased parameter estimates for random excitation signals or when the signal to noise ratio is low. However, by using periodic excitations with high signal-to-noise ratios we were able to avoid these biases.

Parameters for the high-pass filter model were determined by minimizing the  $\chi^2$  between the complex valued transfer function

model and the 225 deg s<sup>-1</sup> sum of sines. The minimization was performed using a Nelder–Mead simplex algorithm implemented by the MATLAB `fminsearch` function (Lagarias et al., 1998). The transfer function was first visually matched to provide initial parameter estimates. We then performed a large iterative parameter sweep around these initial estimates to determine the starting parameters for the minimization runs. The parameters estimates yielding the lowest  $\chi^2$  were used in the final model. There was strong convergence in the final parameter estimates with >10% of runs settling within the same local minimum.

In order to validate our choice of model, we fit a variety of high-pass filter models of different orders to the data. The models were compared using the corrected Akaike's information criterion ( $AIC_c$ ), defined as:

$$AIC_c = \chi^2 + 2k_\theta + \frac{2k_\theta(k_\theta + 1)}{n - k_\theta - 1}, \quad (3)$$

where  $k_\theta$  is the number of model parameters and  $n$  is the number of frequencies (Akaike, 1987; Burnham and Anderson, 2002). The  $AIC_c$  provides a means of comparing the relative goodness-of-fit of different models while penalizing models for the number of parameters. A detailed discussion of the different models and their  $AIC_c$  values is included in the Appendix.

#### Mechanical perturbation experiments

While the abdominal angle (relative to the thorax) was measured in the behavioral experiments, the control signal used by the model was the torque applied at the thoracic–abdominal joint. Because the torque is manifest as an angle change (with some dynamics), we could estimate the torque by measuring the dynamic properties of the joint.

The parameters and dynamics of the control model were primarily derived from simple, direct measurements (e.g. masses) or extrapolated from known values (e.g. moments of inertia). However, measuring the hinge joint dynamics was more complicated and required some assumptions about the properties of the joint. Mathematically, we modeled these dynamics as a torsional spring–damper system. In order to test these assumptions and measure the spring constant and damping coefficient of the hinge joint, we performed a set of mechanical perturbation experiments.

Moths were tethered and placed in the arena, but instead of being presented a visual stimulus they were allowed to ‘fly’ freely in the dark. As they were flying, the abdomen was perturbed from its rest position *via* a physical impulse. An experimenter positioned their hand behind the moth for the entire recording period and applied the impulse by flicking the abdomen with their finger. Moths were then killed using ethyl acetate and reattached to the tether, after which we measured the passive dynamics of the joint using similar perturbations.

Analysis was performed by aligning the maximum abdominal deflection for each impulse. Impulses were selected for analysis only if the abdomen was contacted for a single frame. For trials measuring the passive properties of the joint, the (damped) natural frequency was calculated by measuring the time between subsequent peaks or troughs. The coefficient of damping was calculated by fitting the peak (or minimum) amplitudes with a decaying exponential.

#### Control model

After measuring the visual–abdominal transfer function underlying the response, we determined the efficacy of the behavioral responses for flight control. Specifically, we evaluated whether the extrapolated torque responses, filtered through the

modeled body dynamics of the moth (plant, Fig. 1A), would be sufficient to stabilize the model flight kinematics. We derived the equations of motion for a simplified model of a moth (Fig. 1C) and analyzed the effectiveness of the behaviorally measured transfer function using the Mathematica software package (Wolfram Research, Champaign, IL, USA) and the MATLAB Control Systems toolbox.

The simplified moth model consisted of two masses, an abdomen and a thorax/head combination (Fig. 1C). The abdomen was modeled as an ellipse with major axis  $2l_a$ , a minor axis  $r_a$  and a center of mass  $m_a$ . The thoracic segment was composed of two rigidly fixed circular masses, a head and a true thorax, with radii  $r_{th}$  and  $r_h$  and masses  $m_{th}$  and  $m_h$ , respectively. For simplicity, the coupled masses are simply referred to as the thorax, with combined mass  $m_t$  and radius  $r_t$ .

The abdomen and thorax rotated about a fixed hinge joint, at distances  $l_a$  and  $l_t$  from their respective centers of mass. These rotations were characterized by the angular deflection of the major axes of each mass relative to the horizontal,  $\theta_a$  and  $\theta_t$ , for the abdomen and thorax, respectively. Counterclockwise rotations were defined as positive. Moments of inertia for an ellipse (abdomen,  $I_a$ ) and two fixed circles (thorax,  $I_t$ ) were calculated for rotations around the joint. The lift force of the wings,  $F_w$ , was modeled as an average constant force located along the major axis of the thorax at a distance  $d$  from the hinge joint and oriented at an angle  $\alpha$  relative to the thoracic angle ( $\theta_t$ ). The center of mass of the whole system,  $M$ , was calculated from the positions of the abdominal and thoracic masses.

Real moths control the relative abdominal angle through the actions of muscles at the thoracic–abdominal joint. Conservation of angular momentum requires that changes in the abdominal angle are, in the absence of external forces, balanced by equal and opposite inertial reactions of the thorax. For the model, the abdominal and thoracic angles were modulated by a torque ( $\tau$ ) that acted with equal but opposite direction on the two masses. Because the lift vector was fixed relative to the thorax, changes in joint angle redirected the direction of the lift force. Shifting the center of mass relative to the center of lift also changed the moment arm of the lift forces.

To determine the stability of the system, we first derived the nonlinear Euler–Lagrange equations of the system in the center of mass reference frame:

$$\frac{d}{dt} \frac{\partial}{\partial \dot{q}} L(q, \dot{q}) - \frac{\partial}{\partial q} L(q, \dot{q}) = \tau, \tag{4}$$

where the Lagrangian ( $L$ ) is defined as the difference between the kinetic ( $T$ ) and potential ( $V$ ) energy of the system such that  $L=T-V$ . The vector  $q$  contains the kinematic variables for the system moving and rotating in the  $x$ – $y$  plane,  $q=(x, y, \theta_a, \theta_t)$ , where  $x$  and  $y$  correspond to the horizontal and vertical positions (respectively) of the center of mass ( $M$ ) of the moth. The right-hand side of the equation specifies the internal dynamics of the system while the left-hand side contains the external forces acting on the system. In this case, the external inputs were the torque,  $\tau$ , acting on the hinge joint and the constant wing forces,  $F_w$ , fixed at 90 deg relative to the major axis of the thorax.

The Euler–Lagrange equations for the simulated moth can be expressed in the form:

$$M(q)\ddot{q} + C(q, \dot{q}) + N(q) = \tau + \Gamma, \tag{5}$$

which can be rewritten as:

$$\ddot{q} = M(q)^{-1} [\tau + \Gamma - C(q, \dot{q}) - N(q)]. \tag{6}$$

The mass matrix  $M(q)$  is composed of inertial terms,  $C(q, \dot{q})$  includes Coriolis terms and position- and velocity-dependent constraints,  $N(q)$  includes gravitational terms and  $\Gamma$  represents the generalized forces from the wings.

By substituting out  $q$  for the state vector,  $z$ , defined as:

$$z = \begin{bmatrix} z_1 \\ z_2 \end{bmatrix}, \tag{7a}$$

$$z_1 = \begin{bmatrix} x \\ y \\ \theta_a \\ \theta_t \end{bmatrix}, z_2 = \begin{bmatrix} \dot{x} \\ \dot{y} \\ \dot{\theta}_a \\ \dot{\theta}_t \end{bmatrix}, \tag{7b}$$

the two second-order Lagrange equations (Eqn 4) can be expressed as four first-order equations:

$$\dot{z} = f(z, u) = \begin{bmatrix} z_2 \\ M(z_1)^{-1} [\tau + \Gamma - C(z_1, z_2) - N(z_1)] \end{bmatrix}. \tag{8}$$

Table 1. Model parameter values

Parameter	Symbol	Value
Distance from the hinge joint (m)	$d$	0.006
Lift force of the wings (mN)	$F_w$	17.9
Moment of inertia of an ellipse (abdomen) ( $g\ m^2$ )	$I_a$	$3.9 \times 10^{-4}$
Moment of inertia of an ellipse (thorax) ( $g\ m^2$ )	$I_t$	$1.8 \times 10^{-4}$
Distance from the abdomen to the center of mass (m)	$l_a$	0.0153
Distance from the thorax to the center of mass (m)	$l_t$	0.008
Mass of the abdomen (g)	$m_a$	0.999
Mass of the head (g)	$m_h$	0.106
Mass of the thorax (true thorax + head) (g)	$m_t$	0.832
Mass of the true thorax (g)	$m_{th}$	0.726
Minor axis (m)	$r_a$	0.0055
Radius of the head (m)	$r_h$	0.002
Radius of the thorax (true thorax + head) (m)	$r_t$	0.008
Radius of the true thorax (m)	$r_{th}$	0.006
Angle of wing lift forces (deg)	$\alpha$	90

Masses and lengths were borrowed from Hedrick and Daniel (Hedrick and Daniel, 2006).

The equations of motion for the simple, non-forced, system (Fig. 1C) are then:

$$M(q) = \begin{bmatrix} m_a + m_t & 0 & 0 & 0 \\ 0 & m_a + m_t & 0 & 0 \\ 0 & 0 & \frac{l_a^2 m_a m_t + I_a (m_a + m_t)}{m_a + m_t} & \frac{l_a l_t m_a m_t \cos[\theta_a(t) + \theta_t(t)]}{m_a + m_t} \\ 0 & 0 & \frac{l_a l_t m_a m_t \cos[\theta_a(t) + \theta_t(t)]}{m_a + m_t} & \frac{l_t^2 m_a m_t + I_t (m_a + m_t)}{m_a + m_t} \end{bmatrix}, \quad (9)$$

$$C(q, \dot{q}) + N(q) = \begin{bmatrix} 0 \\ g(m_a + m_t) \\ \frac{l_a l_t m_a m_t \sin[\theta_a(t) - \theta_t(t)] \dot{\theta}_t^2(t)}{m_a + m_t} \\ \frac{l_a l_t m_a m_t \sin[\theta_a(t) - \theta_t(t)] \dot{\theta}_t^2(t)}{m_a + m_t} \end{bmatrix}, \quad (10)$$

The generalized forces,  $\Gamma$ , were determined by mapping the wing forces,  $F_w$ , into joint space by multiplying  $F_w$  by the Jacobian transpose of the position vector at which the force was applied:

$$\Gamma = \begin{bmatrix} F_w \cos[\alpha + \theta_t(t)] \\ F_w \sin[\alpha + \theta_t(t)] \\ \frac{F_w l_a m_a \sin[\alpha - \theta_a(t) + \theta_t(t)]}{m_a + m_t} \\ \frac{F_w [-l_t m_t + d(m_a + m_t)] \sin(\alpha)}{m_a + m_t} \end{bmatrix}, \quad (11)$$

Both the wing forces and gravity were constant over time, leaving the joint torque,  $\tau$ , as the only time-varying control input to the system. The torque acted on the abdominal and thoracic angles with equal, but opposite, magnitudes. To simulate the inherent dynamic properties of the thoracic–abdominal joint, we modeled the joint as a torsional spring–damper system, with spring constant  $k$  and coefficient of damping  $b$ . The abdomen was assumed to have a natural rest angle  $\theta_0$ , defined as the angle at which the spring and gravitational constants balanced to position the center of mass directly under the center of lift. Real moths manipulate the thoracic–abdominal joint angle *via* muscle actuation, which we modeled as a control torque at the joint,  $u_1$ . The net torque at the joint was then:

$$\tau = \begin{bmatrix} 0 \\ 0 \\ u_1 - k[-\theta_0 + \theta_1(t) - \theta_2(t)] - b[\dot{\theta}_1(t) - \dot{\theta}_2(t)] \\ -u_1 + k[-\theta_0 + \theta_1(t) - \theta_2(t)] + b[\dot{\theta}_1(t) - \dot{\theta}_2(t)] \end{bmatrix} \cdot \mathbf{z}_1. \quad (12)$$

These equations constituted the complete nonlinear dynamics of the model moth. The final step for evaluating the model was to input physical parameter values. To be consistent with previous studies, empirical parameter values were borrowed from previous work (Hedrick and Daniel, 2006) and are shown in Table 1.

To simplify the stability analysis, we evaluated the model at an equilibrium state of hovering flight. This simplification allowed for a linear approximation of the full nonlinear equations of motion.

Prior to linearizing the model, we also dropped states that were of minimal interest to our analysis. The model was translation invariant, meaning that the  $(x, y)$  states were decoupled from the rest of the system and could be removed with no loss of generality. The average lift forces were constant to first order near the hovering equilibrium, meaning that acceleration terms in the  $y$  (vertical) direction were zero. Because the moth started at equilibrium (zero vertical motion), this condition meant that the  $\dot{y}$  state could be ignored. Taken together, therefore, these conditions allowed the removal of the  $(x, y, \dot{y})$  terms from the equations of motion. Linearization and stability analyses were then performed on this simplified five-state system.

## RESULTS

### Open-loop system identification

Vertical movements of the abdomen accurately tracked the rotation of the visual pattern, as can be seen in the example data traces (Fig. 2). This tracking is particularly clear for the sum of sines, where the frequency peaks in the abdominal responses closely match those of the visual stimulus (Fig. 2A, center column). A notable exception appears around 20 Hz, where the average signal power increases dramatically. This increased power is attributable to the filtering of the 20–25 Hz wing beat through the thorax and abdomen. Additional low-amplitude spikes present only in the abdominal response traces are likely due to harmonics of the base frequency responses.

The input–output properties of a linear system are fully described by two frequency-dependent variables: the gain, defined as the amplitude ratio of the output over the input, and the phase lag, defined as differences in the relative timing of periodic input and output signals. This input–output relationship can be represented compactly with a transfer function that can then be used to predict the steady-state output of the system to arbitrary inputs.

For these experiments, the input was the angle of the visual pattern, and the output was the abdominal angle. In order to derive a single transfer function from the data, the gain and phase from individual trials were averaged across trials. The transfer function was fit to the averaged response for the lowest-amplitude stimulus, 225 degs<sup>-1</sup>, because it showed the highest similarity between the sum of sines and chirps and did not appear to saturate at high frequencies (discussed in the following section). The average phase and gain for sum of sines and chirp trials are shown in Fig. 3 in the form of a Bode plot.

Abdominal responses are strongly attenuated at frequencies below 1 Hz, after which they plateau as frequency increases. The shape of the gain response is similar for both the chirp and sum of sines and is characteristic of a high-pass filter. The phase plot shows a pronounced, approximately linear, phase roll-off as frequency increases (the roll-off appears to be super-linear due to the log scale on the abscissa). This linear roll-off is indicative of a fixed time delay between the stimulus and response. However, a fixed time delay will not impact the gain of the response. Taken together, the decreased gain at low frequencies and the approximately linear phase

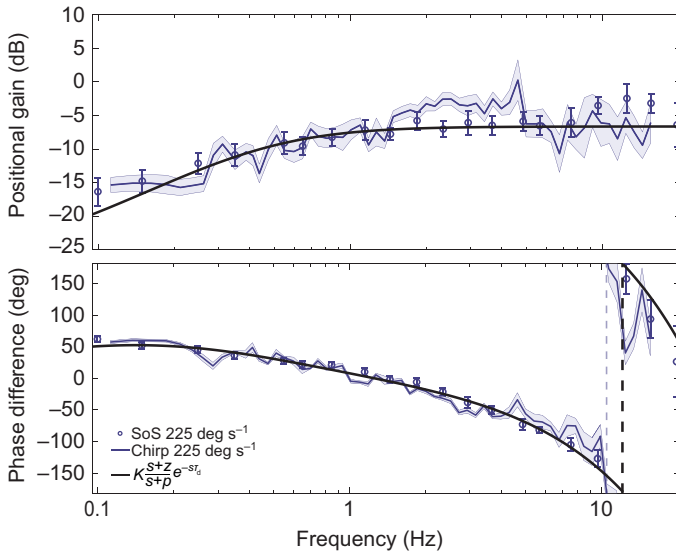


Fig. 3. Gain and phase of the visual–abdominal response. The gain (top) and relative phase (bottom) of the visual–abdominal response is plotted for a single amplitude,  $225 \text{ deg s}^{-1}$ , for sum of sines (SoS; blue circles) and chirp stimuli (blue line). Phase is plotted from  $-180$  to  $180 \text{ deg}$  because of the uncertainty inherent in estimating a periodic variable from data where, for example, phase differences of  $180$  and  $540 \text{ deg}$  are equivalent. Hence, the discontinuities in the phase plot, demarcated by dashed lines, are in fact continuous and are simply the result of the phase rolling off to the next cycle. For these plots, gain and phase were calculated for each trial and then averaged across trials. Error bars and shaded regions represent the 95% confidence intervals for 12 sum of sines trials and 20 chirp trials from seven moths with one to six trials per moth. The data are well described by a high-pass filter function (black line) with a time delay  $\tau_d$  of  $41 \text{ ms}$ .

roll-off suggested that the visual–abdominal transfer function could be modeled by a first-order high-pass filter with a fixed time delay.

To verify our choice of transfer function, we fit multiple different high-pass filter models to the data (see Appendix). Parameters were determined by minimizing the  $\chi^2$  of the model relative to the experimental data as discussed in the Materials and methods. The best model, as determined using the  $\text{AIC}_c$ , was a first order high-pass filter with gain  $K=0.46$ , one zero  $z=0.1\pi$ , one pole  $P=1.0\pi$  and a fixed time delay of  $\tau_d=0.041 \text{ s}$  with a  $\chi^2=48$ . In the Laplace domain, the function has the form:

$$G(s) = \left( K \frac{s+z}{s+p} \right) e^{-s\tau_d}, \quad (13)$$

where  $s$  is the complex frequency ( $\text{rads}^{-1}$ ). The high-pass filter portion of the equation above is the parenthetical term and determines the shape of the gain function. It also influences the phase. The effect of the time delay, specified by the exponential term, is limited to the phase plot only and is manifest as a linear increase in the phase lag with increasing frequency (or as an exponential phase roll-off in the log frequency plot in Fig. 3).

This transfer function was estimated for moths with unrestrained heads. Because moths could track the pattern with head movements, potentially decreasing the apparent motion of the visual stimulus, we also tested two moths with restrained heads. The results (Fig. 4) show that while the shape of the curve remains the same, the gain increases at mid-range frequencies, and a slight, positive shift in the phase response is present at low frequencies.

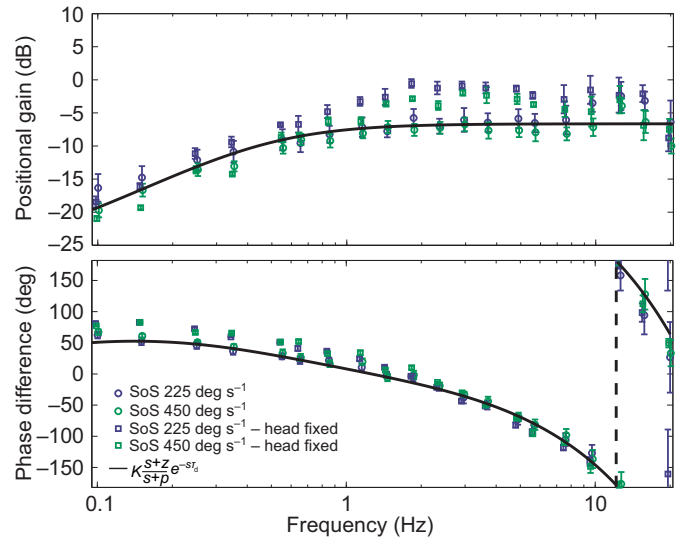


Fig. 4. Comparison of head-fixed and non-head-fixed responses. The gain (top) and relative phase (bottom) of the visual–abdominal response is plotted for two amplitudes of sum of sines (SoS),  $225 \text{ deg s}^{-1}$  (blue) and  $450 \text{ deg s}^{-1}$  (green), for head-fixed (square,  $N=2$  moths,  $n=3$  trials) and non-head-fixed (circle,  $N=8$ ,  $n=22$ ) moths. Error bars represent the 95% confidence intervals. Note the increased gain for head-fixed moths at frequencies above  $1 \text{ Hz}$  and the slight phase shift at low frequencies. The data are well described by a high-pass filter function (black line) with a time delay  $\tau_d$  of  $41 \text{ ms}$ .

#### Response linearity and time invariance

Three amplitudes were tested in chirp experiments. Two amplitudes,  $225$  and  $450 \text{ deg s}^{-1}$ , were used for sum of sines trials because of the longer time course of sum of sines experiments ( $80 \text{ s}$  for sum of sines compared with  $40 \text{ s}$  for chirps).

The results (Fig. 5A; supplementary material Fig. S1) suggest that the visual–abdominal response scales approximately linearly across the threefold amplitude range tested. The response consistency across stimuli types demonstrates that both superposition and time invariance are satisfied. Slight deviations are apparent at low amplitudes where gain varies inversely with stimulus amplitude. At high frequencies and amplitudes, gain drops off for the chirp stimuli, but not for the sum of sines. The phase responses are very consistent, with the exception of the chirp data at high frequencies. These inconsistencies at high frequencies follow from the presence of variability between trials at frequencies beyond the roll-off, partially resulting from the lower signal-to-noise ratio at high frequencies introduced by the wing beat (see Materials and methods). Thus, phase is not reliably computed under those conditions.

The gain differences at low frequency are partially explained by response saturation. The positional amplitudes of visual stimuli were high at low frequencies. Because the visual stimuli wrapped around the edges of the circular arena, there were no limits on the displacement of the grating. The range of abdominal motion, however, had physical limits. Hence, the limited displacement of the abdomen at high stimulus amplitudes necessarily resulted in some nonlinearity in the gain functions measured at low frequencies.

Similarly, the deviation between the sum of sines and chirp results at high frequency is likely due to velocity amplitude saturation. While the velocity maxima were approximately matched between the two types of stimuli, the instantaneous amplitude at any given frequency of the chirp was larger than for the equivalent sum of

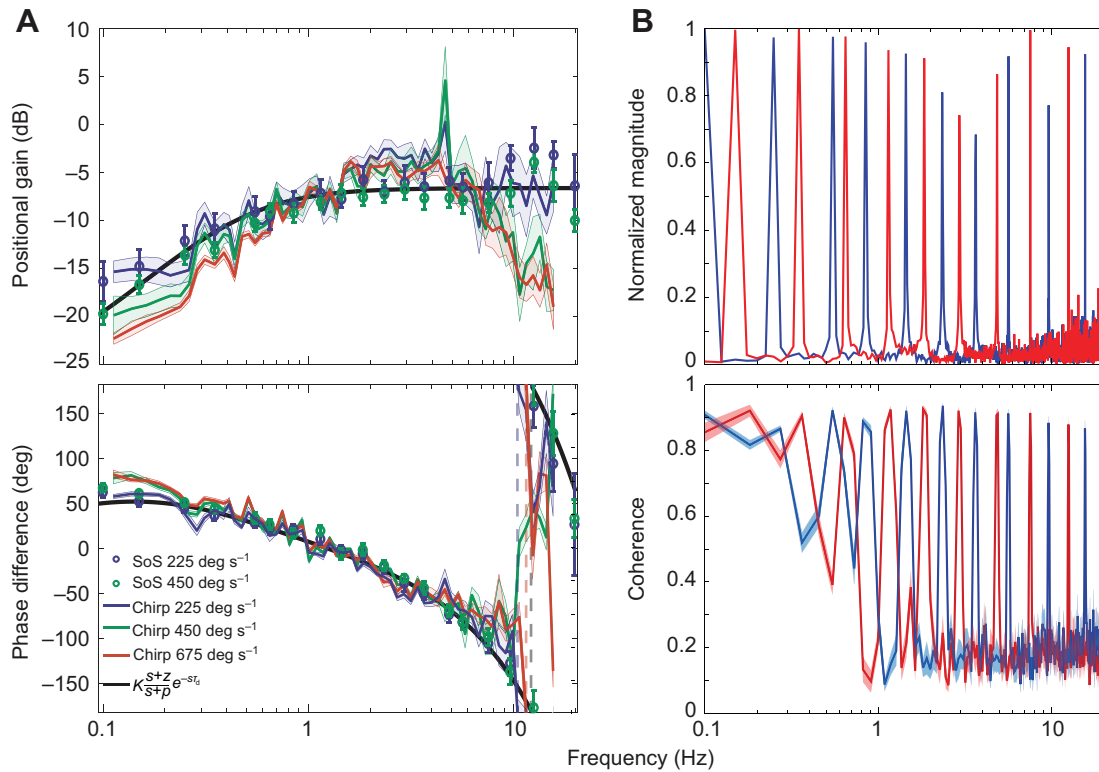


Fig. 5. Measures of system linearity. (A) The gain (top) and relative phase (bottom) plots of the visual–abdominal response were compared for two different amplitudes of sum of sines (SoS) stimuli, 225 deg s<sup>-1</sup> (blue circles,  $N=7$  moths,  $n=12$  trials) and 450 deg s<sup>-1</sup> (green circles,  $N=8$ ,  $n=22$ ), and three different amplitudes of chirp stimuli, 225 deg s<sup>-1</sup> (blue line,  $N=7$ ,  $n=20$ ), 450 deg s<sup>-1</sup> (green line,  $N=6$ ,  $n=22$ ) and 675 deg s<sup>-1</sup> (red line,  $N=7$ ,  $n=30$ ) with one to eight trials per moth. The similarity of the plots across amplitudes strongly suggests that the response is linear within the threefold amplitude range. The estimated transfer function (black line) and low-amplitude data are the same as in Fig. 3. (B) The frequency peaks in the normalized Fourier transform of two interlaced sum of sines trials (top, red and blue lines) correspond to regions of high coherence between the visual stimulus and the abdominal response (bottom). Shaded regions denote the 95% confidence intervals of the averaged coherence of the 450 deg s<sup>-1</sup> sum of sines trials. The high coherence corresponding to the frequency peaks in the stimuli suggest a linear relationship between the visual stimulus and abdominal response.

sines stimulus. This difference is because the sum of sines stimuli contained multiple simultaneous frequency components, so that each individual component had lower amplitude. Hence, the response differences can be explained by a visual saturation non-linearity at the high chirp amplitudes, a fact that is supported by the strong agreement at low chirp amplitudes.

A second test of linearity was provided by the spectral coherence. The coherence was measured for all sum of sines trials and then averaged across trials at the same amplitudes. Coherence was not calculated for the chirp stimuli because the relatively low power at individual frequencies confounded the coherence estimates.

The coherence curve for the 450 deg s<sup>-1</sup> sum of sines trials is shown in Fig. 5B and is consistent with the curves at other amplitudes. As can be seen, the coherence is above 0.8 for all but one of the stimulus peaks. The one exception is the peak around 20 Hz. This difference is likely due to contamination from the ~20 Hz wing beat frequency. The high coherence suggests that the input–output relationship from visual stimulus to abdominal deflection is consistent with a linear model.

#### Mechanical perturbation experiments

The recoveries of three moths to mechanical perturbations of the abdomen are plotted in Fig. 6. The moths recover to within 5 deg of the initial position 100 ms after the perturbations, with subsequent oscillations quickly damped out. An additional low-frequency

recovery from the 5 deg offset to the initial position occurs over the next 200 ms. These results indicate that, during flight, the thoracic–abdominal joint is both stiff (rapid passive response) and close to critically damped and that, to good approximation, the applied torque and angle are approximately linearly related (with some gain).

Dead moths displayed weakly damped abdominal oscillations in response to perturbations. The measured passive properties of the dead moths were consistent with a spring-damped system with natural frequency  $\omega_0=65.8\pm 9.6$  s<sup>-1</sup>, damped natural frequency  $\omega_0=63.0\pm 8.7$  s<sup>-1</sup>, damping ratio  $\zeta=0.267\pm 0.025$  and time constant  $\tau_p=17.4\pm 1.3$  s<sup>-1</sup>.

#### Control model

Having characterized the open-loop visual–abdominal response, we evaluated the effectiveness of the response for maintaining stability during free flight by deriving the full nonlinear equations of motion for a model moth (Fig. 1C).

The perturbation experiments indicated that the thoracic–abdominal joint was heavily damped. Furthermore, the quick recovery to the original abdominal angle suggested that the abdominal angle was specified by a positional command. Hence, it was unnecessary to include the detailed hinge dynamics in the model, as the control signal sent to the abdomen was effectively converted to an angular position. Mathematically, we

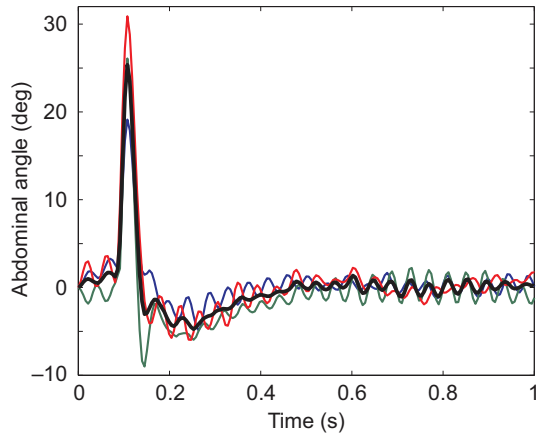


Fig. 6. Abdominal perturbation response during tethered flight. The average abdominal angle in response to a physical perturbation is plotted *versus* time for three individual moths (colored traces) and for the population (black line). After the initial perturbation, the abdominal angle rapidly undershoots (possibly due to passive mechanisms) and then slowly recovers (possibly due to neural feedback).

implemented this by making the control torque,  $u_1$ , a linear function of abdominal angle:

$$u = ku_1, \tag{14}$$

where  $u$  is a new angular control variable. The spring constant  $k$  was then locked to the damping coefficient  $b$ , and the limit of the state equations (Eqn 12) was taken as  $b \rightarrow \infty$ . This limit simplifies the temporal dynamics such that the torque is linearly related to the abdominal angle by a scalar factor  $k$  and, hence, a Hookean process. With this final assumption, the model parameters were fully specified.

The full equations were reduced from an eight- to a five-state system as described in the Materials and methods. The control potential of the abdomen was derived for a specific regime, hovering flight, which allowed linearization of the model about a stable equilibrium. The equilibrium was defined by setting the initial  $x$  and  $y$  positions and velocities to zero. The abdominal and thoracic angles were chosen such that the center of mass was positioned directly beneath the center of lift, as described in the Materials and methods. The system was then linearized by taking the Taylor expansion of the state equations about the equilibrium condition. The first-order terms of the expansion yielded a set of linear equations that approximated the full dynamics of the system.

The transfer function from the input  $u_1$  (proportional to  $\theta_a - \theta_t$ ) to the thoracic (pitch) angle in Laplace space was:

$$P(s) = K_m \frac{s^2 + z_m^2}{s^2}, \tag{15}$$

where  $K_m = -0.69$  and  $z_m^2 = 279 \text{ s}^{-2}$ . This transfer function can also be expressed as an ordinary differential equation in time:

$$\ddot{\theta}_t(t) = K_m (\ddot{u}(t) + z_m^2 u(t)). \tag{16}$$

The transfer function exhibits two temporal scales. One is on the time scale of the position change of the abdomen relative to the thorax, redirecting the lift vector relative to the center of mass. The other time scale is associated with the rotation of the body as a whole in response to that redirection of force.

**Effectiveness of abdomen for flight control**

The above experiments provided two transfer functions, one for the open-loop tethered flight experiments and a second for the closed-loop free flight model. These transfer functions correspond to the sensor/controller blocks and the plant block in the full feedback system (Fig. 1A), respectively. For two linear systems, we can determine the closed-loop dynamics of the combined system from the dynamics of the open-loop components.

The assumption of linearity was well supported by the experimental data. However, combining the two transfer functions required reconciling potential differences between the abdominal dynamics of a tethered moth, as in the case of the experimentally measured transfer function, and for the free-flight case. The dynamics of the sensory input, controller output and plant dynamics will be different for a moth with closed-loop control of the visual stimulus, free-flight body dynamics, or both.

The simplification of the hinge joint dynamics suggested the tethered abdominal response dynamics were a reasonable approximation for the free-flight case. In the behavioral experiments, we measured the transfer function from visual angle to abdominal angle. Because the thorax was fixed to the tether such that the thoracic angle could not be changed, we equated the experimentally measured abdominal angle to the model control input,  $u_1$ , proportional to  $\theta_a - \theta_t$ . As discussed above, the perturbation experiments support the assumption of a positional controller.

Given these caveats, the resulting closed-loop transfer function  $H(s)$  was:

$$H(s) = \frac{G(s)P(s)}{1 + G(s)P(s)}. \tag{17}$$

The time delay makes explicitly evaluating the stability of the system challenging. A graphical method for determining the stability of a time-delayed, linear time-invariant system is the Nyquist plot (Fig. 7). In a Nyquist plot, the stability of the closed-loop system  $H(s)$  is determined by evaluating the open-loop transfer function,  $G(s) \cdot P(s)$ , along the imaginary axis. For a given minimal phase open-loop transfer function (as in our case), the resulting closed-loop system is stable if and only if the  $-1$  point on the real axis is not encircled. For our open-loop system, the product of the experimentally measured transfer controller transfer function  $G(s)$  and the plant model  $P(s)$ , we see that the system does not encircle

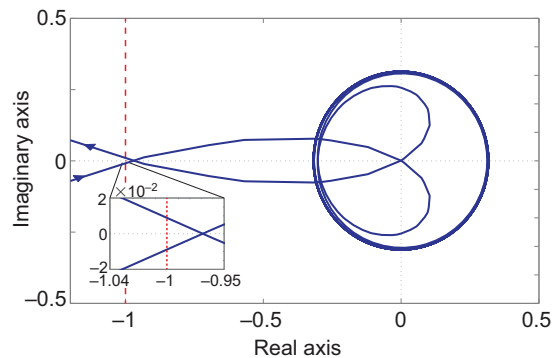


Fig. 7. Nyquist plot for the combined controller–plant feedback system,  $G(s) \cdot P(s)$ . The Nyquist plot provides a graphical method for determining the stability of a time-delayed, closed-loop system. The system is stable if the transfer function, evaluated from  $0 \rightarrow \infty$  along the imaginary axis, does not encircle the  $-1$  point on the real axis (red dashed line). The closeness of the  $-1$  axis to being encircled for this system indicates that abdominal motions contribute to flight stability.

the  $-1$  point and is thus stable. However, the proximity of the crossing-point to  $-1$  suggests that the system is only stable by a small margin, such that a slight increase in the gain could potentially destabilize the system. The magnitude of the decrease required to make the system unstable was smaller than the difference in gain between head-fixed and non-head-fixed moths.

## DISCUSSION

Our results suggest that moths actively modulate their body shape to control flight in response to visual pitch stimuli. By measuring the visual–abdominal sensorimotor transform of a tethered moth using broadband visual stimuli, we showed that the behavioral responses were approximately linear within the range of stimuli we provided. The linearity of the response allowed us to determine the control potential of the abdominal response using a control theoretic model of a hovering moth. The model suggests that movements of the abdomen contribute to pitch stability during flight, but at relatively slow time scales (over multiple wing beats) and with a very slim stability margin. Operating at the edge of stability may allow the animal to quickly transition away from stable, steady-state hovering to agile, unstable maneuvers.

### The transform of visual sensory input to motor output is linear with an approximate delay of 41 ms

We define the sensorimotor transform (or transfer function) as the input–output relationship from visual image position to abdominal angle. Diagrammatically, the behaviorally measured transfer function combines both the sensor and the controller (Fig. 1A) and encompasses a number of different physiological processes, including phototransduction, neural signal propagation and muscle activation.

In measuring the sensorimotor transform, we found that abdominal movements tracked the frequency peaks in the visual stimuli (Fig. 2), which was particularly clear for the discrete peaks present in the sum of sines stimuli. This matching indicated that the behavioral responses were directly related to the motions of the visual pattern (as opposed to some ancillary behavior), allowing us to estimate the sensorimotor transfer function.

In many cases, our stimulus choices differed greatly from previous studies and explain the differences between our observation and previous results. One notable difference was our choice to scale the positional amplitude with frequency, thereby keeping the velocity range of the visual stimuli constant. Previous behavioral results suggested that visual–abdominal responses resembled a band-pass filter, with a peak response at 3 Hz that rolled off on either side (Hinterwirth and Daniel, 2010). These results were consistent with electrophysiological recordings from directionally selective interneurons in the moth brain (Theobald et al., 2010). Our results show that moths are able to respond to frequencies up to, and possibly exceeding, 20 Hz, with our ability to test higher frequencies limited by the wing beat. Responses at frequencies greater than 3 Hz suggest that the response saturation observed in previous studies may be due to the high velocities of the patterns rather than the high temporal frequencies. However, one consequence of fixing the stimulus velocity is that it will have very large positional amplitudes at low frequencies. The variation between the low-frequency responses across amplitudes suggests that there was some response saturation, but that it was limited to the lowest frequencies and yielded rather minor differences. The effects of sensor saturation would likely be more dramatic at higher amplitudes.

The broad frequency sampling allowed us to estimate the visual–abdominal transfer function. We fit the data with a simple first-

order high-pass filter with a fixed delay ( $\tau_d$ ), consistent both with the shape of the gain curve and the phase roll-off. Our model comparison results demonstrated that reducing the number of model parameters, particularly the pole or the delay, significantly reduced the goodness-of-fit of the model, while higher-order models added unnecessary complexity without increasing the predictive power (see Appendix, Table A1).

By fitting our model in the frequency domain we were able to disambiguate the effects of the high-pass filter and the fixed time delay on phase. This delay, likely due to signal transmission and/or encoding times, appears as a phase lag that increases linearly with temporal frequency (Fig. 3). Phase lags can result both due to a fixed time delay, which results from characteristics such as signal propagation delays, and/or due to filtering (or neural processing), so that attempts to estimate the time delay at a single frequency will almost certainly yield spurious estimates. Quantifying the behavioral delay is critically important because shifts in response latency have significant ramifications for control, with longer delays decreasing the stability margin of a system.

Our estimated transfer function was composed of a high-pass filter multiplied by a fixed time delay (exponential term in Eqn 13). Based on our model fit, we measured an estimated time delay,  $\tau_d$ , of 41 ms. While we are unable to quantify the precision of this estimate, given the multiple parameters in our estimated transfer function and the variance of our data, 2–3 ms changes in this parameter noticeably impact the  $\chi^2$ . While this behavioral delay is consistent with other measures of response delays of visually mediated behaviors in other insects (Heisenberg and Wolf, 1988; Robert and Rowell, 1992), it is somewhat surprising given that the moths in our study were dark adapted, which can increase photoreceptor response times by up to 30 ms (Howard et al., 1984). The delay is also notably different from the 100–200 ms response delays measured from visual interneurons (Theobald et al., 2010). That difference may arise from an unknown behavioral state in fixed preparations that are necessary for intracellular recordings. Supporting this conclusion is the fact that we did not observe abdominal motions when moths were not actively flapping their wings, indicating that the response was dependent on the behavioral state of the animal. In addition, in one experimental trial not included in our analyses, we measured a time delay of  $\sim 100$  ms (supplementary material Fig. S2). A second set of experiments on the same moth yielded a time delay of  $\sim 40$  ms, indicating that the moth was capable of responding more quickly to the visual stimulus. This change in time delay may be evidence for the importance of the behavioral state or attention of the animal on behavioral output.

The 41 ms delay in the abdominal response indicates that it is a relatively slow control mechanism, acting at the time scale of individual wing strokes. This time scale would suggest that the abdomen is unlikely to play a significant role in the recovery from fast ( $<40$  ms) flight perturbations, or at least in the initial phase of the recovery. However, it is not clear whether this time delay is limited by sensory processing, or is instead reflective of the relative time scale of control in which the abdomen is involved. Previous experiments in *M. sexta* have shown that abdominal reflexes can be elicited by both mechanical and visual stimuli (Hinterwirth and Daniel, 2010).

The majority of our experiments were performed with moths that were free to move their heads. Moths clearly moved their heads in phase with the visual pattern and head motion could affect the resulting optic flow. Unlike abdominal movements, head movements were apparent even when moths were not actively flapping their wings. Although unrestrained head preparations created a potential

confound for measuring the visual–abdominal transfer function, the condition was more relevant to free flight where insects use head motions to actively stabilize their gaze (Huston and Krapp, 2008; van Hateren and Schilstra, 1999). The head-fixed experiments indicated that, while eliminating head motions did alter the abdominal response, the changes were mainly in the gain of the response. This result makes intuitive sense, as the apparent visual motions across the eye were greater when moths were not able to partially compensate for the motion by visually tracking pattern movement.

All physiological processes are nonlinear over a sufficiently large parameter space and, as mentioned previously, the measured sensorimotor transform encompassed multiple, presumably nonlinear (e.g. Howard et al., 1984), physiological processes (Fig. 1A). However, we show that the visual–abdominal response is time-invariant and satisfies the two conditions for linearity, superposition and scaling, within a restricted parameter space and during steady-state behavior. Comparison of the sum of sines and chirp responses (Fig. 3, Fig. 4A) demonstrates that the responses to sequentially presented single frequencies (chirps) are consistent with the responses to the frequencies superimposed (sum of sines). The constant gain between amplitudes (Fig. 5A) indicates linear scaling between the input visual stimulus and the abdominal output. Time invariance is shown by the response consistency between both different sum of sines stimuli with randomized phase, and between sum of sines and chirps. These two properties, linearity and time invariance, were necessary in order to derive a general transfer function describing the behavioral output to an arbitrary input and, hence, integral to the stability analyses.

While it was surprising that the combination of multiple nonlinear processes underlying the visual–abdominal response yielded a linear transfer function, this observation is not unprecedented, with linearity in behavioral responses having been previously observed for both behavioral outputs (Roth et al., 2011) and the integration of sensory inputs (Frye and Dickinson, 2004; Hinterwirth and Daniel, 2010). The fact that biological systems, with their fundamentally nonlinear underpinnings, display linear behavior is not as surprising as one might think. The system is operating near an equilibrium, and nonlinear dynamics can be reasonably represented by linear dynamics in the regions of attraction of equilibria (Åström and Murray, 2008).

### Control and stability

By measuring the sensorimotor transfer function from visual input to abdominal output, we were able to determine the potential role of abdominal movements for flight control. As previously mentioned, the experimentally measured transfer function corresponded to the combined sensor/controller block of our control theoretic model (Fig. 1A). In order to determine the effects of the outputs of the controller on flight control, we first needed to relate the output of the sensorimotor transfer function, in the form of an abdominal angle, to the input to the plant, a muscle activation or torque. Our mechanical perturbation experiments (Fig. 6) suggested that these two quantities were linearly related. In order to relate the torque inputs to the kinematic output, and thereby test the contribution of abdominal motions to flight stability, we needed to derive a transfer function for the plant. Because the physical plant dynamics were nonlinear, we linearized them around a stable hovering equilibrium, yielding a transfer function that could be inserted into the model. Combining the two transfer functions (Eqn 17) yielded a linear, time-invariant system upon which we could perform stability analyses.

The recovery of the abdomen to its initial angle during the tethered flight perturbation experiments was fast, especially when compared with the time constant of recovery of the dead moth. There are two possible explanations for this rapid recovery during tethered flight that are not mutually exclusive: active muscle may be tuned to reject mechanical perturbations, and/or rapid, active reflexes at the thoracic–abdominal joint are involved. The slower, secondary recovery from mechanical perturbations that we observed also suggested that the moth may be sensing its abdominal position. This conclusion is not unreasonable given the quantities of sensors that most animals possess, as well the importance of proprioception. Given the large mass of the abdomen, and its resulting resistance to acceleration, it is possible that it could serve as a large proof mass for an inertial sensor. This characteristic would mean that the abdomen could be serving as an actuator, governing movement, and also a sensor, detecting the state of the animal in the environment. Such nonlinear coupling between sensation and actuation is often observed in biology, but it rarely appears in human-engineered systems. Investigating this interplay, and the potential advantages of actively moving the sensors, is one area where biological sciences can provide insight and inspiration to engineering.

The linearized plant model (Eqn 16) revealed two mechanisms by which abdominal motions could influence flight path. The first is due to the shifting of the center of mass relative to the centers of lift and thrust, altering the rotational moment of the moth, and has been previously proposed as a possible control mechanism during flight and aerial descent (Hedrick and Daniel, 2006; Libby et al., 2012; Zanker, 1988a). The second is the physical redirection of lift vector on the thorax when the joint is flexed. To our knowledge, this mechanism of action has not been previously proposed and would be unique to flying animals that are actively generating lift and thrust forces. The possible advantages of redirecting forces through abdominal flexion, as opposed to simply altering the aspects of the wing kinematics, are unclear. A sustained change in abdominal angle could provide a straightforward method for trimming the direction of the wing forces.

This apparent redundancy also highlights the fact that animals are true multiple-input–multiple-output (MIMO) systems. It is likely that the abdomen works synergistically with the wings for flight control. Given the relatively low frame rates of our cameras, we were unable to fully reconstruct wing motions. However, previous experiments by Hinterwirth and Daniel (Hinterwirth and Daniel, 2010) have shown that abdominal responses work in concert with the wings. A potentially valuable and interesting future research direction would be to measure the transfer functions of both the wings and the abdomen to visual input and determine whether the actions of the two are complementary for stability. Our hypothesis would be that they work together, but that the temporal bandwidth of the responses is likely different, with the wings acting relatively quickly and the abdomen working at a slower time scale.

For simplicity, we modeled the action of the wings as a constant force vector oriented at a fixed angle relative to the thorax. However, we did not consider the aerodynamic forces produced by the periodic forcing of the wings, which may strongly influence the temporal dynamics of the body during flapping flight. Studies applying computational fluid dynamics techniques to moth flight have shown that cyclic wing forcing introduces an aerodynamic pitching moment that results in unstable longitudinal motions when the moth is perturbed during hovering flight (Sun et al., 2007). Our results

suggest that abdominal motions could play a role in counteracting this instability, but such a conclusion would require detailed consideration of both the aerodynamics of flapping flight as well as the phase of abdominal movements relative to the wing beat cycle. We do not believe that these aerodynamic effects qualitatively impact our conclusions, but the nonlinear effects could have significant impacts on our control analyses, and the stability margin, of our model.

Our experiments investigated abdominal control of pitch, but moths also display weaker abdominal reflexes about the yaw and roll axes (Hinterwirth and Daniel, 2010). Pitch motions were of particular interest to us because of the moths' inherent instability about this axis (Sun et al., 2007; Sane et al., 2007), suggesting that pitch stabilization requires active neural feedback. Furthermore, the symmetry of the moth about the pitch axis made the plant dynamics more tractable from a mathematical standpoint. The abdomen likely plays an important role in the control of yaw and roll, but the dynamics are much more complicated due to the coupling of yaw and roll moments during abdominal deflections and asymmetries in the insect about these axes.

Recent work with freely hovering moths has shown that the abdominal motions during free flight are consistent in direction with those observed in our tethered preparation (Cheng et al., 2011). The time delay of the abdominal flexion, relative to pitch angle, appeared to be much faster, on the order of 20 ms. The faster time scale lends credence to our hypothesis that mechanosensory information also mediates abdominal responses.

While our experiments suggest that the abdomen plays a role in flight control, we could not determine the relative importance of the abdomen for flight control. Hedrick and Daniel (Hedrick and Daniel, 2006) indirectly addressed this issue using an inverse modeling approach, in which they investigated the parameters necessary to achieve a desired kinematic state. In the case of stable hovering flight, they did not show a clear role for abdominal movements. However, this does not preclude abdominal contributions to flight control or that the abdomen may be more important for control at longer time scales. Our results are consistent with this hypothesis, as the abdomen appeared to have a relatively slow time scale of control (on the order of multiple wing beats).

Our results suggest that abdominal motions help stabilize flight and that the resulting feedback system was very close to the stability margin. The margin was small enough that slight changes in gain or delay of the controller, such as those resulting from fixing the head, could make the system unstable. One disadvantage of highly stable systems is that they are resistant to change such that any changes in state can require significant energy and time. By skirting the stability margin, the system could easily shift into an agile, unstable regime that would increase the animal's maneuverability. Here we define maneuverability as the availability of high rates of change for switching between states. While our results are consistent with this strategy, it is possible that the transfer function during closed-loop behavior could shift further away from the stability margin, further stabilizing (or destabilizing) the system. Additional measurements of the visual-abdominal input-output relationship during tethered closed-loop or free-flight experiments would help determine the operating stability margin during natural behavior. Despite these caveats, this work points to a powerful strategy for increasing flight agility in which sensory-motor systems are maintained at the stability margin to allow quick transitions between stable and maneuverable states.

## APPENDIX

### Model comparisons

A total of six different models were fit to the abdominal response data. Because the response data displayed high-pass filter behavior, we chose to test high-pass filter models of different orders with and without time delays. The six models were:

$$G_1(s) = K_1 \frac{s}{s + p_1}, \quad (A1)$$

$$G_2(s) = K_2 \frac{s + z_2}{s + p_2}, \quad (A2)$$

$$G_3(s) = \left( K_3 \frac{s}{s + p_3} \right) e^{-s\tau_3}, \quad (A3)$$

$$G_4(s) = \left( K_4 \frac{s + z_4}{s + p_4} \right) e^{-s\tau_4}, \quad (A4)$$

$$G_5(s) = \left( K_5 \frac{s}{(s + p_{5a})(s + p_{5b})} \right) e^{-s\tau_5}, \quad (A5)$$

$$G_6(s) = \left( K_6 \frac{s + z_6}{(s + p_{6a})(s + p_{6b})} \right) e^{-s\tau_6}, \quad (A6)$$

where the  $K_i$  terms denote gains, the  $z_i$  terms are zeros, the  $p_i$  terms are poles, the  $\tau_i$  terms are delays and  $s$  is the complex frequency in the Laplace domain (units of  $\text{rad s}^{-1}$ ).

Parameters for the models were determined by minimizing the  $\chi^2$  of the model relative to the 225  $\text{deg s}^{-1}$  sum of sines data as described in the Model fit section of the Materials and methods. Because the size of the parameter space for the higher-order models was so large, initial parameters for each model were determined by first manually fitting the models to the data. We then performed very large parameter sweeps around these initial values to settle on the best-fit parameter choices. The final parameters and  $\chi^2$  values for each model are shown in Table A1 and the Bode plots for the different models are shown in Fig. A1.

Using the best-fit parameter values for each model, we then evaluated the relative goodness-of-fit of each model using Akaike's information criterion (AIC), which provides an estimate of the relative loss of information between different models (Burnham and Anderson, 2002). The AIC is easily calculated using the  $\chi^2$  as follows:

$$\text{AIC} = \chi^2 + k_0, \quad (A7)$$

where  $k_0$  is the number of model parameters (Akaike, 1987). A smaller AIC is better and, as can be seen from the equation, the AIC penalizes models for the number of parameters. Hence, while a high-order model that fits the data better can always be found (until the parameters exceed the degrees of freedom of the data), these parameters come at the cost of making the model more

Table A1. Parameter and goodness-of-fit metrics for each of the high-pass filter models (Eqns A1–A6)

	$G_1$	$G_2$	$G_3$	$G_4$	$G_5$	$G_6$
$K_i$	0.31	0.31	0.45	0.46	-119	-84
$\tau_i$	–	–	0.041	0.041	0.45	0.47
$z_i$	–	-0.011 $\pi$	–	0.1 $\pi$	–	0.1 $\pi$
$p_{ai}$	0.38 $\pi$	0.36 $\pi$	0.78 $\pi$	1.0 $\pi$	-84 $\pi$	-57 $\pi$
$p_{bi}$	–	–	–	–	0.79 $\pi$	0.97 $\pi$
$\chi^2$	787	787	59	48	59	47
AIC <sub>G</sub>	792	795	66	59	69	61
$L$	0	0	0.02	1.0	0	0.25

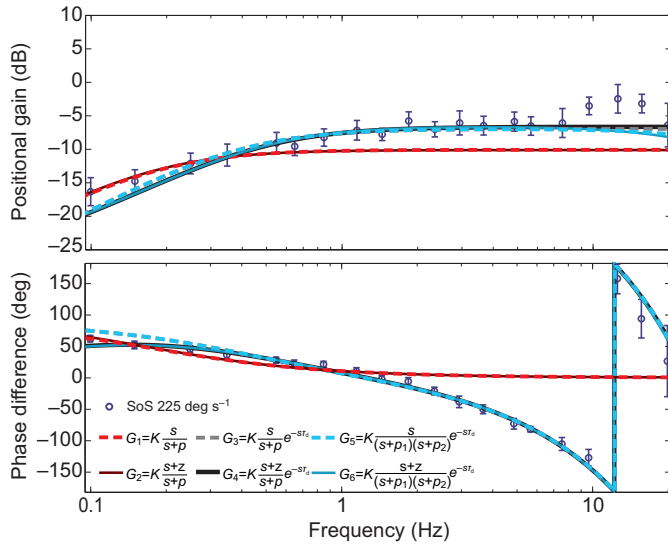


Fig. A1. Transfer function model comparison Bode plot. (A) The transfer functions for the six different high pass filter models fit to the 225 deg s<sup>-1</sup> sum of sines (SoS) data (blue circles,  $N=7$  moths,  $n=12$  trials) with the 95% confidence intervals computed in the complex plane (Roth et al., 2011). Equations for the different models, with zeros  $z$ , poles  $p$  and time delays  $\tau_d$ , are provided in the figure. The models without time delays (red lines) do a poor job fitting the phase at high frequencies, which indirectly impacts the magnitude curve due to the least squares error minimization used to fit the model parameters. The models without zero parameters (dashed lines) do a poorer job of fitting the phase at lower frequencies.

complex. It is also important to note that the values of the AIC are only informative relative to other models.

The AIC will be biased for a model with a large number of parameters relative to samples, as was the case for our study with a maximum  $k_0=5$  and  $n=20$  frequency samples. To account for this in our model comparison, we calculated the corrected AIC (AIC<sub>c</sub>, Eqn 3) for each model (Table A1). We were also able to calculate the relative likelihood  $L$  of each model:

$$L = e^{\frac{\text{AIC}_{c,\text{min}} - \text{AIC}_{c,i}}{2}} \quad (\text{A8})$$

The relative likelihood indicates how probable a model is to minimize information loss compared with the minimum AIC (AIC<sub>c,4</sub>), and values for the six models are shown in Table A1. For instance, model  $G_6$  is 0.25 times as likely to minimize the information loss as model  $G_4$ .

#### ACKNOWLEDGEMENTS

We would like to thank Armin Hinterwirth for his help with the virtual flight arena, Eatai Roth for his assistance with the stimulus design and data analysis, Billie Medina for her assistance working with the moths, and Simon Sponberg for his helpful input and feedback.

#### AUTHOR CONTRIBUTIONS

J.P.D., T.L.D. and N.J.C. conceived and designed the experiments. J.P.D. performed the behavioral experiments. J.P.D. and N.J.C. developed the model and performed the analyses. J.P.D., T.L.D. and N.J.C. interpreted the results. J.P.D., K.A.M., T.L.D. and N.J.C. wrote the paper.

#### COMPETING INTERESTS

No competing interests declared.

#### FUNDING

This material is based upon work supported by the National Science Foundation under a Postdoctoral Research Fellowship in Biology [no. 1103768 to J.P.D.] and grant nos EEC-1028725 (to T.L.D.) and CISE-0845749 (to N.J.C.); the Office of Naval Research under grant no. N000141010952 (to K.A.M. and T.L.D.); the Air Force Research Laboratory as part of the DARPA HI-MEMS program (T.L.D. and J. Voldman); and a Komen Endowed Chair to T.L.D.

#### REFERENCES

- Akaike, H. (1987). Factor analysis and AIC. *Psychometrika* **52**, 317-332.
- Åström, K. J. and Murray, R. M. (2008). *Feedback Systems: An Introduction for Scientists and Engineers*. Princeton, NJ: Princeton University Press.
- Bendat, J. S. and Piersol, A. G. (1980). *Engineering Applications of Correlation and Spectral Analysis*. New York, NY: Wiley-Interscience.
- Berens, P. (2009). CircStat: a MATLAB toolbox for circular statistics. *J. Stat. Softw.* **31**, 1-21.
- Burnham, K. P. and Anderson, D. R. (2002). *Model Selection and Multi-Model Inference: a Practical Information-Theoretic Approach*. New York, NY: Springer.
- Camhi, J. M. (1970a). Sensory control of abdomen posture in flying locusts. *J. Exp. Biol.* **52**, 533-537.
- Camhi, J. M. (1970b). Yaw-correcting postural changes in locusts. *J. Exp. Biol.* **52**, 519-531.
- Cheng, B., Deng, X. and Hedrick, T. L. (2011). The mechanics and control of pitching manoeuvres in a freely flying hawkmoth (*Manduca sexta*). *J. Exp. Biol.* **214**, 4092-4106.
- Dyhr, J. P., Cowan, N. J., Colmenares, D. J., Morgansen, K. A. and Daniel, T. L. (2012). Autostabilizing airframe articulation: animal inspired air vehicle control. In *2012 IEEE 51st Annual Conference on Decision and Control (CDC)* pp. 3715-3720. USA: IEEE. doi: 10.1109/CDC.2012.6426256
- Frye, M. A. and Dickinson, M. H. (2004). Motor output reflects the linear superposition of visual and olfactory inputs in *Drosophila*. *J. Exp. Biol.* **207**, 123-131.
- Götz, K. G., Hengstenberg, B. and Biesinger, R. (1979). Optomotor control of wing beat and body posture in *Drosophila*. *Biol. Cybern.* **35**, 101-112.
- Hateren, J. H. and Schilstra, C. (1999). Blowfly flight and optic flow. II. Head movements during flight. *J. Exp. Biol.* **202**, 1491-1500.
- Hedrick, T. L. (2008). Software techniques for two- and three-dimensional kinematic measurements of biological and biomimetic systems. *Bioinspir. Biomim.* **3**, 034001.
- Hedrick, T. L. and Daniel, T. L. (2006). Flight control in the hawkmoth *Manduca sexta*: the inverse problem of hovering. *J. Exp. Biol.* **209**, 3114-3130.
- Heisenberg, M. and Wolf, R. (1988). Reafferent control of optomotor yaw torque in *Drosophila melanogaster*. *J. Comp. Physiol. A* **163**, 373-388.
- Hinterwirth, A. J. and Daniel, T. L. (2010). Antennae in the hawkmoth *Manduca sexta* (Lepidoptera, Sphingidae) mediate abdominal flexion in response to mechanical stimuli. *J. Comp. Physiol. A* **196**, 947-956.
- Howard, J., Dubs, A. and Payne, R. (1984). The dynamics of phototransduction in insects. *J. Comp. Physiol. A* **154**, 707-718.
- Huston, S. J. and Krapp, H. G. (2008). Visuomotor transformation in the fly gaze stabilization system. *PLoS Biol.* **6**, e173.
- Lagarias, J. C., Reeds, J. A., Wright, M. H. and Wright, P. E. (1998). Convergence properties of the nelder-mead simplex method in low dimensions. *SIAM J. Optim.* **9**, 112-147.
- Libby, T., Moore, T. Y., Chang-Siu, E., Li, D., Cohen, D. J., Jusufi, A. and Full, R. J. (2012). Tail-assisted pitch control in lizards, robots and dinosaurs. *Nature* **481**, 181-184.
- Luu, T., Cheung, A., Ball, D. and Srinivasan, M. V. (2011). Honeybee flight: a novel 'streamlining' response. *J. Exp. Biol.* **214**, 2215-2225.
- McCormack, A. S., Godfrey, K. R. and Flower, J. O. (1994). The detection of and compensation for nonlinear effects using periodic input signals. In *Proceedings of the International Conference on Control, 1994*, pp. 297-302. USA: IEEE.
- Pintelon, R. and Schoukens, J. (2012). *System Identification: A Frequency Domain Approach*. New York, NY: IEEE Press.
- Reiser, M. B. and Dickinson, M. H. (2008). A modular display system for insect behavioral neuroscience. *J. Neurosci. Methods* **167**, 127-139.
- Robert, D. and Rowell, C. H. F. (1992). Locust flight steering. *J. Comp. Physiol. A* **171**, 41-51.
- Roth, E., Zhuang, K., Stamper, S. A., Fortune, E. S. and Cowan, N. J. (2011). Stimulus predictability mediates a switch in locomotor smooth pursuit performance for *Eigenmannia virescens*. *J. Exp. Biol.* **214**, 1170-1180.
- Sane, S. P., Dieudonné, A., Willis, M. A. and Daniel, T. L. (2007). Antennal mechanosensors mediate flight control in moths. *Science* **315**, 863-866.
- Sun, M., Wang, J. and Xiong, Y. (2007). Dynamic flight stability of hovering insects. *Acta Mech. Sin.* **23**, 231-246.
- Taylor, J. R. (1997). *An Introduction to Error Analysis*, 2nd edn. Sausalito, CA: University Science Books.
- Taylor, G. K. (2001). Mechanics and aerodynamics of insect flight control. *Biol. Rev. Camb. Philos. Soc.* **76**, 449-471.
- Theobald, J. C., Warrant, E. J., and O'Carroll, D. C. (2010). Wide-field motion tuning in nocturnal hawkmoths. *Proc. R. Soc. Lond. B* **277**, 853-860.
- Zanker, J. M. (1988a). On the mechanism of speed and altitude control in *Drosophila melanogaster*. *Physiol. Entomol.* **13**, 351-361.
- Zanker, J. M. (1988b). How does lateral abdomen deflection contribute to flight control of *Drosophila melanogaster*? *J. Comp. Physiol. A* **162**, 581-588.